Viscous second gradient porous materials for bones reconstructed with bio-resorbable grafts

Ivan Giorgio, Ugo Andreaus, Francesco Dell 'Isola, Tomasz Lekszycki

Viscous second gradient porous materials for bones reconstructed with bio-resorbable grafts

Ivan Giorgio[a,c,*], Ugo Andreaus[a], Francesco dell'Isola[a,c], Tomasz Lekszycki[b,c]

[a] *Dep. of Structural and Geotechnical Engineering, Università di Roma La Sapienza 18 Via Eudossiana, Rome, Italy*
[b] *Warsaw University of Technology, Warsaw, Poland*
[c] *International Research Center for the Mathematics and Mechanics of Complex Systems - MeMoCS, Università dell'Aquila Cisterna di Latina, Italy*

Abstract

It is well known that size effects play an important role in the mechanical behavior of bone tissues at different scales. In this paper we propose a second gradient model for accounting these effects in a visco-poro-elastic material and present some sample applications where bone is coupled with bioresorbable artificial materials of the kind used in reconstructing surgery.

Keywords: Metamaterials, second gradient materials, porous media, viscous dissipation, bone remodelling
2010 MSC: 00-01, 99-00

1. Introduction

Substantial size effects are known to occur in the elastic behavior of (i) single osteons [1], (ii) human compact bone [2, 3, 4, 5, 6, 7], (iii) human trabecular bone [8, 9]. In the first case, the size effects are attributed to compliance of the interfaces between laminae. In the second case, there is experimental evidence that the cement lines as compliant interfaces account for most of the difference in stiffness between osteons and whole bone. In the third case, continuum properties vary by more than 20-30% over a distance spanning three to five trabeculae and hence a continuum model for the structure is suspect [8]. Therefore, Ramézani et al. [9] used the Cosserat theory to describe the hierarchical multi-scale behavior of trabecular human bone using micro-CT images, namely: i) macroscale, dealing with cancellous bone or spongy bone at real size; ii) meso-scale, representing non-homogeneous and stochastic network clusters; iii) micro-scale, indicating the micro-randomness and heterogeneous deformations; iv) sub-micro- and nano-scale, showing single lamellas including collagen fibers and apatite crystals. Generally speaking, the limitations of the continuum assumption appear in two areas: near biologic interfaces, and where there are large stress gradients. To incorporate the scale of the microstructure of a heterogeneous material within the continuum framework, a number of phenomenological 'remedies' have been proposed that involve the relaxation of the local action hypothesis of classical continuum mechanics. Such enriched (or enhanced) continuum models aim at including information on the microstructure and can be classified into three main groups [10], namely: (i) non-local integral models [11, 12, 13], (ii) higher-order gradient models [14, 15, 16] and (iii) micropolar theories [17, 18, 19]. Bleustein [20] showed how the boundary conditions of a linear theory of an elastic continuum with microstructure [21] can be reduced to those of a corresponding linear form of a strain gradient theory [22]. Following this way of thinking, second gradient materials can be interpreted as a particular limit case of micromorphic (or micropolar) media because they can be deduced from micromorphic ones by constraining the micromorphic kinematic descriptors to be equal to the classical strain ones by introducing internal constraints and Lagrange multipliers. We remark that this constrained approach which is rigorous in a finite-dimensional space, it is assumed reasonably acceptable in an infinite-dimensional space on the basis of an argument of analogy. This paper is inspired by the more general framework of a research oriented to design the mechanical characteristics of the biomaterial constituting the graft, namely mass density and resorption velocity, in order to optimize the mass density distribution of the growing bone tissue. From the above it is clear the importance of size effects in mechanical behavior of bone tissues and biomaterials, since one can think of achieving them with a structure similar to that of bone tissue. Thus, in this paper we intend to take these size effects into account by formulating a constitutive model that includes the use of the displacement

*Corresponding author
Email address: ivan.giorgio@uniroma1.it (Ivan Giorgio)

gradients higher than the first one.

2. Material and methods

The considered specimen is constituted by the union of two bi-dimensional square portions, one constituted of bone tissue and the other of biomaterial; the square size is $L/2 = W = 0.5$ cm. The mass densities of the two materials are initially assigned in each zone and they will evolve in the subsequent remodeling process according to the mechanical and biological laws presented in the following (see Eq. (17)). The support conditions on one edge are shown in a self-explanatory way in Fig. 1. A traction distribution corresponding to a pure bending is applied to the opposite edge as shown in Fig. 1; the load is harmonically variable with a low frequency Ω in order to activate the component of the stimulus which is related to dissipation, because this phenomenon plays a key role in the bone functional adaptation, as discussed in [23]. In particular, we set

$$f_b(x_2,t) = \left(\frac{2x_2}{W} - 1\right)[F_0 + F_1 \sin(\Omega t)] \tag{1}$$

Some relevant results will be presented with reference to the probe point P_m in the material zone (Fig. 1).

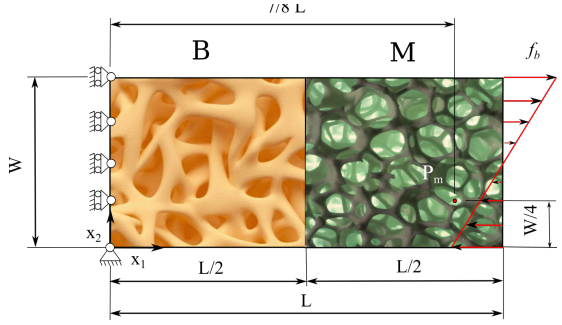

Figure 1: Sample under study at initial stage.

3. Governing Equations

Kinematics. In order to give a macroscopic description of the system under study constituted by an insert of bio-resorbable grafting material and a piece of bone, i.e. a porous mixture, we introduce the placement field:

$$\boldsymbol{\chi} : (\boldsymbol{X}, t) \mapsto \boldsymbol{x} \tag{2}$$

which takes each point of body $\boldsymbol{X}$ in the reference configuration $\mathcal{B}$ and time $t \in \mathbb{R}$ into a place $\boldsymbol{x}$ in the current configuration. Therefore, we consider the solid-matrix macroscopic displacement ($\boldsymbol{u} = \boldsymbol{x} - \boldsymbol{X}$) as a basic kinematical descriptor and use the Saint-Venant strain tensor

$$E_{\mathrm{ij}}(\mathbf{X}, t) = \frac{1}{2}\left(u_{\mathrm{i,j}} + u_{\mathrm{j,i}} + u_{\mathrm{i,k}}\, u_{\mathrm{k,j}}\right) \tag{3}$$

to take elastic deformations into account. Because of the porous nature of our system, we introduce another independent kinematical descriptor to describe the microdeformations of pores inside the solid matrix of the system. In particular, we introduce the change of the Lagrangian porosity, i.e. the change of the effective volume of the fluid content per unit volume of the body with respect to an equilibrium volume [24]. In detail,

$$\zeta(\mathbf{X}, t) = \phi(\boldsymbol{\chi}(\mathbf{X}, t), t) - \phi^*(\mathbf{X}, t) \tag{4}$$

where ϕ and ϕ^* are the Lagrangian porosity related to the current and the reference configuration, respectively. By adopting the approach of the mixture theory, these porosities can be expressed as follows

$$\phi = 1 - (\rho_{\mathrm{b}}/\hat{\rho}_{\mathrm{b}} + \rho_{\mathrm{m}}/\hat{\rho}_{\mathrm{m}}), \quad \phi^* = 1 - (\rho^*_{\mathrm{b}}/\hat{\rho}_{\mathrm{b}} + \rho^*_{\mathrm{m}}/\hat{\rho}_{\mathrm{m}}) \tag{5}$$

where ρ_{b} and ρ_{m} are the apparent mass densities of bone tissue and artificial material, respectively; the superimposed hat denotes the true densities, while the superscript * indicates all quantities in the reference configuration.

Variational equation of motion. For the potential energy-density —potential energy per unit of macrovolume— we take a homogeneous, quadratic function of the variables $\boldsymbol{E}$, $\nabla\boldsymbol{E}$, ζ and $\nabla\zeta$ [21, 25, 26, 15]

$$\begin{aligned}\mathscr{E} = {} & \frac{1}{2}\lambda(\rho^*_{\mathrm{b}}, \rho^*_{\mathrm{m}})\, E_{\mathrm{ii}} E_{\mathrm{jj}} + \mu(\rho^*_{\mathrm{b}}, \rho^*_{\mathrm{m}})\, E_{\mathrm{ij}} E_{\mathrm{ij}} + \\ & 4\,\alpha_1(\rho^*_{\mathrm{b}}, \rho^*_{\mathrm{m}}) E_{\mathrm{ii,j}} E_{\mathrm{jk,k}} + \alpha_2(\rho^*_{\mathrm{b}}, \rho^*_{\mathrm{m}}) E_{\mathrm{ii,j}} E_{\mathrm{kk,j}} + \\ & 4\,\alpha_3(\rho^*_{\mathrm{b}}, \rho^*_{\mathrm{m}}) E_{\mathrm{ij,i}} E_{\mathrm{kj,k}} + 2\,\alpha_4(\rho^*_{\mathrm{b}}, \rho^*_{\mathrm{m}}) E_{\mathrm{ij,k}} E_{\mathrm{ij,k}} + \\ & 4\,\alpha_5(\rho^*_{\mathrm{b}}, \rho^*_{\mathrm{m}}) E_{\mathrm{ij,k}} E_{\mathrm{ik,j}} + \frac{1}{2} K_1(\rho^*_{\mathrm{b}}, \rho^*_{\mathrm{m}})\zeta^2 + \\ & \frac{1}{2} K_2 \zeta_{,\mathrm{i}} \zeta_{,\mathrm{i}} - K_3(\rho^*_{\mathrm{b}}, \rho^*_{\mathrm{m}})\, \zeta\, E_{\mathrm{ii}}\end{aligned} \tag{6}$$

where λ and μ are the Lamé parameters

$$\lambda = \frac{\nu\, Y(\rho^*_{\mathrm{b}}, \rho^*_{\mathrm{m}})}{(1+\nu)(1-2\nu)}, \qquad \mu = \frac{Y(\rho^*_{\mathrm{b}}, \rho^*_{\mathrm{m}})}{2(1+\nu)}, \tag{7}$$

here expressed in terms of the Young modulus of the mixture

$$Y = Y^{\mathrm{Max}}_{\mathrm{b}}(\rho^*_{\mathrm{b}}/\hat{\rho}_{\mathrm{b}})^{\beta_{\mathrm{b}}} + Y^{\mathrm{Max}}_{\mathrm{m}}(\rho^*_{\mathrm{m}}/\hat{\rho}_{\mathrm{m}})^{\beta_{\mathrm{m}}} \tag{8}$$

and Poisson ratio. $Y^{\mathrm{Max}}_{\mathrm{b}}$ and $Y^{\mathrm{Max}}_{\mathrm{m}}$ are the maximal elastic moduli and the exponents β_{b}, β_{m} are constants. The second gradient stiffness coefficients are assumed to be:

$$\begin{aligned}&\alpha_1 = \alpha_2 = \alpha_4 = Y(\rho^*_{\mathrm{b}}, \rho^*_{\mathrm{m}})\ell^2, \ \alpha_3 = 2Y(\rho^*_{\mathrm{b}}, \rho^*_{\mathrm{m}})\ell^2, \\ &\alpha_5 = 1/2 Y(\rho^*_{\mathrm{b}}, \rho^*_{\mathrm{m}})\ell^2\end{aligned} \tag{9}$$

being ℓ a suitable scale length of the microstructure. The coefficient K_1 is a coefficient of compressibility related to the bone marrow inside pores and can be evaluated as

$$K_1 = \left(\frac{\phi^*}{K_{\mathrm{f}}} + \frac{(\alpha_B - \phi^*)(1-\alpha_B)}{K_{\mathrm{dr}}}\right)^{-1} \tag{10}$$

in which K_{f} is the marrow modulus, $K_{\mathrm{dr}} = Y/(3(1-2\nu))$ is the drained bulk modulus of the porous matrix and α_B is the Biot-Willis coefficient. The coupling between microstructure and solid bulk is assumed to be

$$K_3 = \sqrt{\hat{g}(\phi^*)\,\lambda\,K_1} \tag{11}$$

where the weight function

$$\hat{g}(\phi^*) = \frac{A_{k_3}}{\pi}\left\{\operatorname{atan}\left[s_{k_3}\left(\phi^* - \frac{1}{2}\right)\right] + \operatorname{atan}\left(\frac{s_{k_3}}{2}\right)\right\} \tag{12}$$

modulates the micro-macro coupling depending on the reference porosity. The coefficients A_{k_3} and s_{k_3} can be chosen to characterize the coupling law adopted.

To model dissipative phenomena, we employ a Rayleigh dissipation function

$$2\mathcal{D}_s = 2\mu^v\left(\dot{E}_{\mathrm{ij}}\dot{E}_{\mathrm{ij}} - \frac{1}{3}\dot{E}_{\mathrm{ii}}\dot{E}_{\mathrm{jj}}\right) + \kappa^v\,\dot{E}_{\mathrm{ii}}\dot{E}_{\mathrm{jj}} \tag{13}$$

related to the solid-matrix macroscopic rate strain. The material parameters κ^v and μ^v are the bulk and shear viscosity coefficients, respectively.

The Generalized Principle of Virtual Work, including dissipation effects and neglecting inertia terms, for independent variations δu_{i} and $\delta\zeta$, therefore, runs as follows

$$-\int_{\mathcal{B}}\delta\mathscr{E}\,\mathrm{d}\,\mathcal{B} + \int_{\mathcal{B}}\delta\mathscr{W}^{\mathrm{ext}}\mathrm{d}\,\mathcal{B} = \int_{\mathcal{B}}\frac{\partial\mathcal{D}_s}{\partial\dot{E}_{\mathrm{ij}}}\delta E_{\mathrm{ij}}\mathrm{d}\,\mathcal{B} \tag{14}$$

where $\delta\mathscr{W}^{\mathrm{ext}}$ is the variation of the work done by external actions. The assumed potential energy-density (6) is the motivation for the adoption of the following form for the variation of work done by external action:

$$\delta\mathscr{W}^{\mathrm{ext}} = \int_{\partial_\tau\mathcal{B}}\tau_{\mathrm{i}}\delta u_{\mathrm{i}}\mathrm{d}\mathcal{S} + \int_{\partial_\tau\mathcal{B}}T_\alpha\delta u_{\alpha,\mathrm{j}}n_{\mathrm{j}}\mathrm{d}\mathcal{S} + \int_{\partial\mathcal{B}}\Xi\,\delta\zeta\mathrm{d}\mathcal{S}, \tag{15}$$

where body and line forces are neglected, and T_α are double forces per unit of area.

It is worth noting that a second gradient continuum model can be deduced via an homogenization procedure based on micro-macro identification to obtain an equivalent model which reproduces at the macro scale the behaviour of the material characterised by a complex microstructure at micro-scale (see e.g. [30, 16, 31]). In this homogenization process, some critical issues as for instance a damage occuring in the bone tissue or in the biomaterial can be taken into account (see e.g. [27, 28, 29]).

Interface modeling. Interface conditions can be formulated by adding to the energy density (6) an internal boundary extra term:

$$\mathscr{E}_{\mathrm{int}} = \frac{1}{2}K_\zeta\,[\![\zeta]\!]^2 + \frac{1}{2}K_u\,[\![\boldsymbol{u}]\!]\cdot[\![\boldsymbol{u}]\!] + \frac{1}{2}K_{\nabla u}\,[\![(\nabla\boldsymbol{u})\boldsymbol{n}]\!]\cdot[\![(\nabla\boldsymbol{u})\boldsymbol{n}]\!] \tag{16}$$

This simple interface potential energy-density can be useful to better describe the real conditions of connection between bone tissue and artificial material with a proper choice of the stiffnesses K_ζ, K_u and $K_{\nabla u}$, related respectively to ζ, $\boldsymbol{u}$ and $\nabla\boldsymbol{u}$.

Evolution rules. The evolution of the apparent mass densities is governed by the rules [32, 33]:

$$\begin{cases}\dot{\rho}^*_{\mathrm{b}} = A_{\mathrm{b}}(S)\;H(\phi) & \text{with } 0 < \rho^*_{\mathrm{b}} \leqslant \hat{\rho}_{\mathrm{b}}\\ \dot{\rho}^*_{\mathrm{m}} = A_{\mathrm{m}}(S)\;H(\phi) & \text{with } 0 < \rho^*_{\mathrm{m}} \leqslant \rho^*_{\mathrm{m}}(\boldsymbol{X},0)\end{cases} \tag{17}$$

which are assumed to depend on the mechanical stimulus S resulting from an external applied load and the current porosity ϕ. The functions A_{b} and A_{m} are taken to be

$$A_{\{\mathrm{b,m}\}}(S) = \begin{cases} s_{\{\mathrm{b,m}\}}S & \text{for } S \geq 0\\ r_{\{\mathrm{b,m}\}}S & \text{for } S < 0\end{cases} \tag{18}$$

with different constant rates for synthesis (s_{b} and $s_{\mathrm{m}} = 0$) and for resorption (r_{b} and r_{m}). Of course, we remark that the synthesis of bio-resorbable material is not allowed, i.e., $s_{\mathrm{m}} = 0$. The weight function H is characterized by a U-like shape with a maximum in the neighbourhood of $\phi = 0.5$ to emphasize the most effective conditions in the remodelling process. In the definition of the stimulus, the presence of a lazy zone, bounded by two thresholds ($P^{\mathrm{s}}_{\mathrm{ref}}$ and $P^{\mathrm{r}}_{\mathrm{ref}}$ for synthesis and for resorption, respectively), is hypothesized where the osteoregulatory balance of the bone is maintained. Mathematically:

$$S(\boldsymbol{X},t) = \begin{cases} P(\boldsymbol{X},t) - P^{\mathrm{s}}_{\mathrm{ref}} & \text{for } P(\boldsymbol{X},t) > P^{\mathrm{s}}_{\mathrm{ref}}\\ 0 & \text{for } P^{\mathrm{r}}_{\mathrm{ref}} \leqslant P(\boldsymbol{X},t) \leqslant P^{\mathrm{s}}_{\mathrm{ref}}\\ P(\boldsymbol{X},t) - P^{\mathrm{r}}_{\mathrm{ref}} & \text{for } P(\boldsymbol{X},t) < P^{\mathrm{r}}_{\mathrm{ref}}\end{cases} \tag{19}$$

The signal P related to the sensing biological activity is assumed to take the following form [23]:

$$P(\boldsymbol{X},t) = \frac{\int_{\mathcal{B}}\left(\alpha\,\mathscr{E}_s + \ell\,\mathcal{D}_s\right)\varpi\left(\rho^*_{\mathrm{b}}\right)\;e^{-\frac{\|\boldsymbol{X}-\boldsymbol{X}_0\|^2}{2D^2}}\mathrm{d}\boldsymbol{X}_0}{\int_{\mathcal{B}}e^{-\frac{\|\boldsymbol{X}-\boldsymbol{X}_0\|^2}{2D^2}}\mathrm{d}\boldsymbol{X}_0} \tag{20}$$

characterized by a reference length D which delimits the range of action of the biological processes. $\mathscr{E}_s$ is the density of strain energy of the solid matrix (including first and second gradient terms) and $\varpi = \eta\rho^*_{\mathrm{b}}/\hat{\rho}_{\mathrm{b}}$ is the density of active sensor cells assumed to be present only in the living bone tissue.

4. Numerical results

The constitutive model of the second gradient formulated in the previous section has been implemented in a finite element code (COMSOL Multiphysics), optimized for constitutive models of the first gradient. To overcome this limitation, it was decided to find a micromorphic model of the first gradient that was equivalent to the second gradient model, using the technique of Lagrange multipliers [34]. A further improvement can be

achieved employing the recent developed tools of the isogeometric analysis particularly suitable for their inherent high continuity to treat the second gradient models (see for more details e.g. [35, 36, 37, 38]). Starting from an initial apparent mass density uniform for the bone tissue ($\rho_{\rm b}^{*} = 0.5\hat{\rho}_{\rm b}$) and the biomaterial ($\rho_{\rm m}^{*} = 0.5\hat{\rho}_{\rm m}$), we perform a parametric analysis by varying the characteristic length ℓ of the second gradient governed by Eq. (9). The parameters used in the simulations are: $Y_{\rm b}^{\rm Max} = 17$ GPa, $Y_{\rm m}^{\rm Max} = 0.8\,Y_{\rm b}^{\rm Max}$, $\nu = 0.3$, $\hat{\rho}_{\rm b} = \hat{\rho}_{\rm m} = 1800$ kg/m^3, $\beta_{\rm b} = \beta_{\rm m} = 2$, $K_{\rm f} = 0.1\,Y_{\rm b}^{\rm Max}$, $D = 0.1L$, $K_2 = 1.7 \times 10^5$ N, $K_\zeta = 1.7 \times 10^7$ N/m, $K_u = 1.7 \times 10^{18}$ N/m^3, $K_{\nabla u} = 1.7 \times 10^7$ N/m, $\eta = 0.2$, $A_{k_3} = 0.9$, $s_{k_3} = 15$, $\mu^v = 2.57 \times 10^{12}$ N s/m^2, $\kappa^v = 2.06 \times 10^{12}$ N s/m^2, $s_{\rm b} = 1.27 \times 10^{-7}$ s/m^2, $r_{\rm b} = 1.06 \times 10^{-7}$ s/m^2, $r_{\rm m} = 1.59 \times 10^{-7}$ s/m^2, $P_{\rm ref}^{\rm s} = 1.43$ N/m^2, $P_{\rm ref}^{\rm r} = 1.29$ N/m^2, α =1, ℓ= 6.048 $\times 10^6$ s, $F_0 = 2.0 \times 10^{-3}\,Y_{\rm b}^{\rm Max}$, $F_1 = F_0/2$ and $\Omega = 8.27 \times 10^{-7}$ Hz.

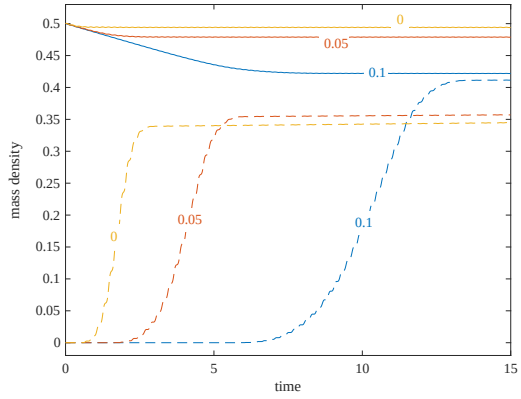

Figure 2: Time evolution of the mass densities of bone (dashed line) and material (solid line) in the probe point P_m when characteristic length ℓ is varying.

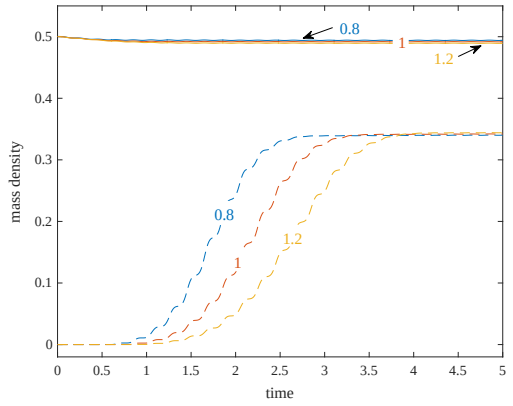

Figure 3: Time evolution of the mass densities of bone (dashed line) and material (solid line) in the probe point P_m when Y_m is varying and $\ell = 0$.

In all the following figures we plot mass densities normalized with respect to the maximum values. In Fig. 2, we compare the model of the first gradient ($\ell = 0L$) with that of the second gradient, for two different values of the characteristic length ($\ell = \{0.05L, 0.1L\}$), as reported close to the respective curves in figure. The three dashed curves refer to the bone, while the three continuous curves relate to the material. It is observed that as the characteristic length increases, the evolutionary process takes place in a longer time and therefore the material undergoes a greater resorption and this entails that the bone has available a greater space to grow. Therefore, in the stationary state, the bone attains a greater mass density (and the material a lesser one) as the characteristic length increases. We note that this behavior is similar to that found in the case of the first gradient (Fig. 3), when increasing values of the maximum Young modulus Y_m of the biomaterial are assumed. In this case, the cause of stiffening is represented by the consideration of the second gradient in the constitutive relation of the mixture.

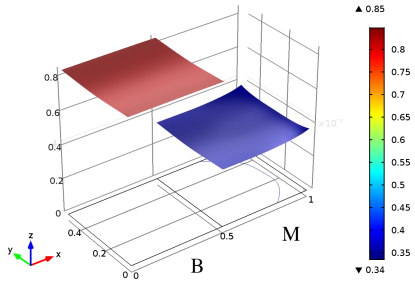

(a)

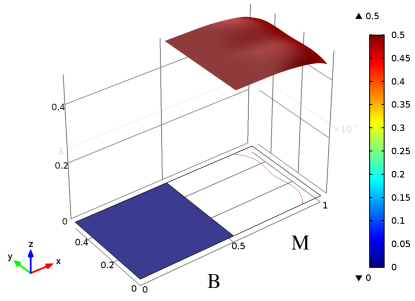

(b)

Figure 4: Distributions of the mass densities of (a) bone and (b) material at the end of the process with $\ell = 0$.

Figure 4 shows the situation at the end of the adaptation process in terms of apparent mass density of bone (Fig. 4a) and biomaterial (Fig. 4b), when the model of the first gradient is used. Figure 4 serves as a reference to compare the results found via the second gradient model, respectively with characteristic lengths $0.05L$ (Fig.5) and $0.1L$ (Fig.6).

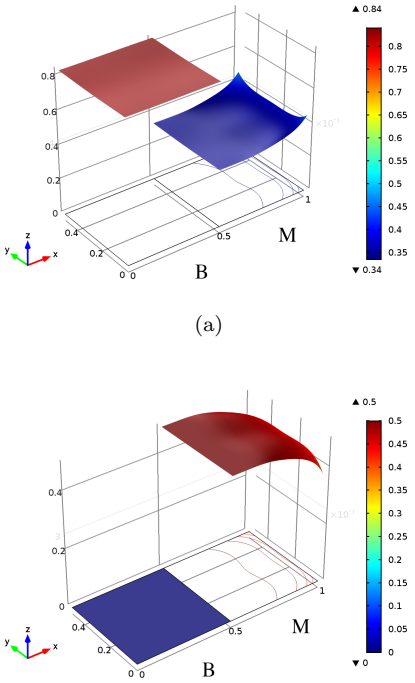

(a)

(b)

Figure 5: Distributions of the mass densities of (a) bone and (b) material at the end of the process with $\ell = 0.05\,L$.

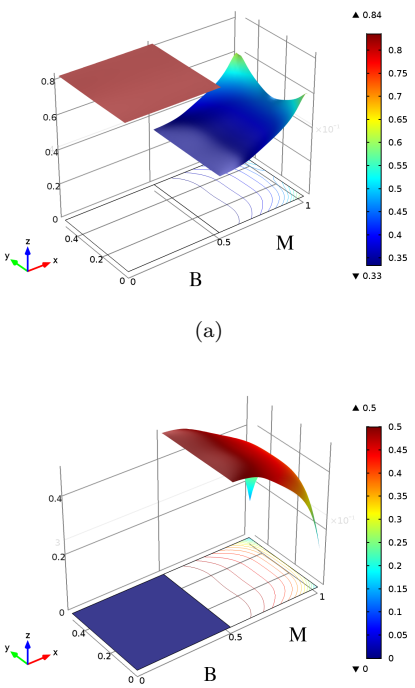

(a)

(b)

Figure 6: Distributions of the mass densities of (a) bone and (b) material at the end of the process with $\ell = 0.1\,L$.

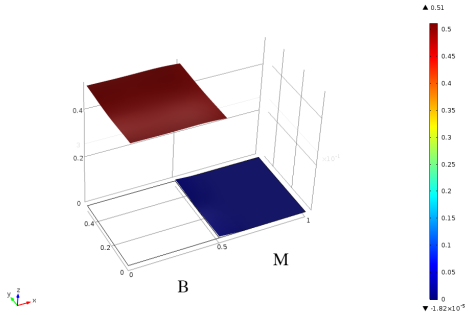

(a)

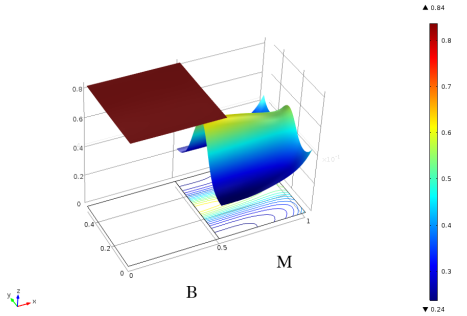

(b)

Figure 7: Distributions of bone mass density at the (a) beginning and (b) end of the process.

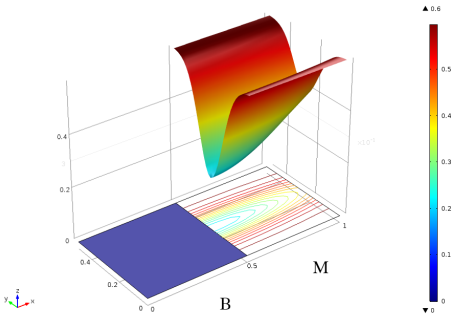

(a)

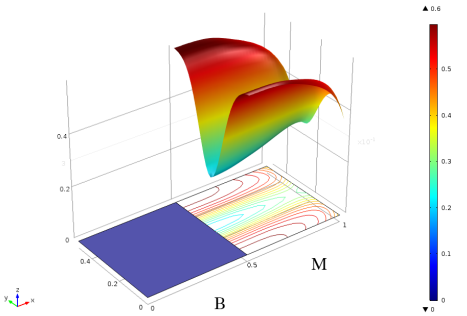

(b)

Figure 8: Distributions of material mass density at the (a) beginning and (b) end of the process.

Figures 5 and 6 show the distributions of the apparent mass density of (a) bone and (b) biomaterial at the end of the process with the second gradient model with $\ell = 0.05L$ (Fig. 5) and $\ell = 0.1L$ (Fig. 6). It can be observed that the main differences are located in the area in the vicinity of the application of load (see Fig. 1) and further from the bone area. The portions of resorbed biomaterial and deposited bone grow with increasing characteristic length. To facilitate the understanding of the distribution of mass density in Figs. 4, 5, and 6, the level curves in plan have been reported too. In order to design the mass density to optimize the distribution of the material, it is thought to reduce the initial mass density in the neighbourhood of the neutral axis (see Fig. 8a), given that the load condition is of bending. Thus, the initial (a) and final (b) states of the remodeling process, both as regards the bone (Fig. 7) and the biomaterial (Fig. 8), were compared in the case in which the initial mass density of the biomaterial is not uniform and the characteristic length is $0.07L$. In the present case the neutral axis is aligned in the longitudinal direction of the sample. It is noted that the biomaterial area with greater porosity constitutes a fast track to the bone penetrating inside the area of the material, which in fact is more dense in the area where the initial density of the biomaterial is lower, having a greater available space.

5. Conclusions

This paper presents a constitutive model for the bone-biomaterial mixture, characterized by taking into account a second gradient model. The aim was to compare the results obtained via a simpler model of the first gradient, noting that the effect of the second gradient is to delay the process of evolution, in a manner similar to what happens when the biomaterial is stiffened under the assumption of first gradient model. This study was done assuming uniform initial mass densities of bone and biomaterial in their respective areas. It is then analyzed the case in which the mass density of the biomaterial is not uniform at the beginning of the process, resulting in a greater bone growth where the rarefaction of the biomaterial allows it.

References

[1] R. Lakes, On the torsional properties of single osteons, J. Biomech. 28 (11) (1995) 1409–1410. doi:10.1016/0021-9290(95)00057-0.

[2] P. Frasca, R. Harper, J. L. Katz, Strain and frequency dependence of shear storage modulus for human single osteons and cortical bone microsamples—size and hydration effects, J. Biomech. 14 (10) (1981) 679–690. doi:10.1016/0021-9290(81)90050-6.

[3] J. F. C. Yang, R. S. Lakes, Transient study of couple stress effects in compact bone: torsion, J Biomech Eng. 103 (4) (1981) 275–279. doi:10.1115/1.3138292.

[4] R. S. Lakes, Dynamical study of couple stress effects in human compact bone, J Biomech Eng. 104 (1) (1982) 6–11. doi:10.1115/1.3138308.

[5] J. F. C. Yang, R. S. Lakes, Experimental study of micropolar and couple stress elasticity in compact bone in bending, J. Biomech. 15 (2) (1982) 91–98. doi:10.1016/0021-9290(82)90040-9.

[6] H. C. Park, R. S. Lakes, Cosserat micromechanics of human bone: strain redistribution by a hydration sensitive constituent, J. Biomech. 19 (5) (1986) 385–397. doi:10.1016/0021-9290(86)90015-1.

[7] P. M. Buechner, R. S. Lakes, Size effects in the elasticity and viscoelasticity of bone, Biomech. Model. Mechanobiol. 1 (4) (2003) 295–301. doi:10.1007/s10237-002-0026-8.

[8] T. P. Harrigan, M. Jasty, R. W. Mann, W. H. Harris, Limitations of the continuum assumption in cancellous bone, J. Biomech. 21 (4) (1988) 269–275. doi:10.1016/0021-9290(88)90257-6.

[9] H. Ramézani, A. El-Hraiech, J. Jeong, C.-L. Benhamou, Size effect method application for modeling of human cancellous bone using geometrically exact cosserat elasticity, Comput. Methods Appl. Mech. Engrg. 237 (2012) 227–243. doi:10.1016/j.cma.2012.05.002.

[10] J. Fatemi, F. Van Keulen, P. R. Onck, Generalized continuum theories: Application to stress analysis in bone, Meccanica 37 (4-5) (2002) 385–396. doi:10.1023/A:1020839805384.

[11] E. Kröner, Elasticity theory of materials with long range cohesive forces, Int. J. Solids Struct. 3 (5) (1967) 731–742. doi:10.1016/0020-7683(67)90049-2.

[12] A. C. Eringen, D. G. B. Edelen, On nonlocal elasticity, International Journal of Engineering Science 10 (3) (1972) 233–248. doi:10.1016/0020-7225(72)90039-0.

[13] F. dell'Isola, U. Andreaus, L. Placidi, At the origins and in the vanguard of peridynamics, non-local and higher-gradient continuum mechanics: An underestimated and still topical contribution of Gabrio Piola, Mathematics and Mechanics of Solids 20 (8) (2015) 887–928. doi:10.1177/1081286513509811.

[14] A. Madeo, D. George, T. Lekszycki, M. Nierenberger, Y. Rémond, A second gradient continuum

model accounting for some effects of micro-structure on reconstructed bone remodelling, C R Mecanique 340 (8) (2012) 575–589. doi:10.1016/j.crme.2012.05.003.

[15] F. dell'Isola, P. Seppecher, A. Della Corte, The postulations á la D'Alembert and á la Cauchy for higher gradient continuum theories are equivalent: a review of existing results, Proc. R. Soc. A 471 (2183) (2015) 20150415. doi:10.1098/rspa.2015.0415.

[16] J.-J. Alibert, A. Della Corte, Second-gradient continua as homogenized limit of pantographic microstructured plates: a rigorous proof, Z. Angew. Math. Phys. 66 (5) (2015) 2855–2870. doi:10.1007/s00033-015-0526-x.

[17] E. Cosserat, F. Cosserat, Théorie des corps déformables, Paris, 1909.

[18] H. Altenbach, V. A. Eremeyev, On the linear theory of micropolar plates, Z. Angew. Math. Mech 89 (4) (2009) 242–256. doi:10.1002/zamm.200800207.

[19] J. Altenbach, H. Altenbach, V. A. Eremeyev, On generalized Cosserat-type theories of plates and shells: a short review and bibliography, Arch. Appl. Mech. 80 (1) (2010) 73–92. doi:10.1007/s00419-009-0365-3.

[20] J. L. Bleustein, A note on the boundary conditions of Toupin's strain-gradient theory, Int. J. Solids Struct. 3 (6) (1967) 1053–1057. doi:10.1016/0020-7683(67)90029-7.

[21] R. D. Mindlin, Micro-structure in linear elasticity, Arch. Rational Mech. Anal. 16 (1) (1964) 51–78. doi:10.1007/BF00248490.

[22] R. A. Toupin, Elastic materials with couple-stresses, Arch. Rational Mech. Anal. 11 (1) (1962) 385–414. doi:10.1007/BF00253945.

[23] I. Giorgio, U. Andreaus, D. Scerrato, F. dell'Isola, A visco-poroelastic model of functional adaptation in bones reconstructed with bio-resorbable materials, Biomech. Model. Mechanobiol.doi:10.1007/s10237-016-0765-6.

[24] M. A. Biot, Mechanics of deformation and acoustic propagation in porous media, J. Appl. Phys. 33 (4) (1962) 1482–1498. doi:10.1063/1.1728759.

[25] L. Placidi, U. Andreaus, A. Della Corte, T. Lekszycki, Gedanken experiments for the determination of two-dimensional linear second gradient elasticity coefficients, Z. Angew. Math. Phys. 66 (6) (2015) 3699–3725. doi:10.1007/s00033-015-0588-9.

[26] F. dell'Isola, G. Sciarra, S. Vidoli, Generalized Hooke's law for isotropic second gradient materials, Proc. R. Soc. A 465 (2009) 2177–2196. doi:10.1098/rspa.2008.0530.

[27] L. Placidi, A variational approach for a nonlinear 1-dimensional second gradient continuum damage model, Continuum Mech Therm 27 (4-5) (2015) 623–638. doi:10.1007/s00161-014-0338-9.

[28] L. Placidi, A variational approach for a nonlinear one-dimensional damage-elasto-plastic second-gradient continuum model, Continuum Mech Therm 28 (1-2) (2016) 119–137. doi:10.1007/s00161-014-0405-2.

[29] A. Misra, V. Singh, Micromechanical model for viscoelastic materials undergoing damage, Continuum Mech Therm 25 (2-4) (2013) 343–358. doi:10.1007/s00161-012-0262-9.

[30] I. Goda, M. Assidi, S. Belouettar, J. F. Ganghoffer, A micropolar anisotropic constitutive model of cancellous bone from discrete homogenization, J Mech Behav Biomed Mater 16 (2012) 87–108. doi:10.1016/j.jmbbm.2012.07.012.

[31] A. Cecchi, N. L. Rizzi, Heterogeneous elastic solids: A mixed homogenization-rigidification technique, Int. J. Solids Struct. 38 (1) (2001) 29–36. doi:10.1016/S0020-7683(00)00018-4.

[32] T. Lekszycki, F. dell'Isola, A mixture model with evolving mass densities for describing synthesis and resorption phenomena in bones reconstructed with bio-resorbable materials, Z. Angew. Math. Mech 92 (6) (2012) 426–444. doi:10.1002/zamm.201100082.

[33] U. Andreaus, I. Giorgio, A. Madeo, Modeling of the interaction between bone tissue and resorbable biomaterial as linear elastic materials with voids, Z. Angew. Math. Phys. 66 (1) (2015) 209–237. doi:10.1007/s00033-014-0403-z.

[34] S. Forest, Micromorphic approach for gradient elasticity, viscoplasticity, and damage, J. Eng. Mech. 135 (3) (2009) 117–131. doi:10.1061/(ASCE)0733-9399(2009)135:3(117).

[35] A. Cazzani, M. Malagù, E. Turco, Isogeometric analysis of plane-curved beams, Math. Mech. Solidsdoi:doi:10.1177/1081286514531265.

[36] A. Cazzani, M. Malagù, E. Turco, F. Stochino, Constitutive models for strongly curved beams in the frame of isogeometric analysis, Math. Mech. Solids 21 (2016) 183–209. doi:10.1177/1081286515577043.

[37] L. Greco, M. Cuomo, An isogeometric implicit G1 mixed finite element for Kirchhoff space rods, Comput Methods Appl Mech Eng 298 (2016) 325–349. doi:10.1016/j.cma.2015.06.014.

[38] L. Greco, M. Cuomo, An implicit G1 multi patch B-spline interpolation for Kirchhoff–Love space rod, Comput Methods Appl Mech Eng 269 (2014) 173–197. doi:10.1016/j.cma.2013.09.018.